Cryo-electron microscopy for structural analysis of dynamic biological macromolecules

BBA - General Subjects 1862 (2018) 324–334

Contents lists available at ScienceDirect

BBA - General Subjects

journal homepage: www.elsevier.com/locate/bbagen

Review

Cryo-electron microscopy for structural analysis of dynamic biological macromolecules☆

Kazuyoshi Murata[a,*], Matthias Wolf[b,*]

[a] National Institute for Physiological Sciences, 38 Myodaiji, Okazaki, Aichi 444-8585, Japan
[b] Molecular Cryo-Electron Microscopy Unit, Okinawa Institute of Science and Technology, 7542 Onna, Onna-Son, Kunigami, Okinawa 904-0411, Japan

ARTICLE INFO

Keywords:
Electron cryomicroscopy
Cryo-electron tomography
Single particle 3D reconstruction
Protein structure
Molecular dynamics

ABSTRACT

Background: Since the introduction of what became today's standard for cryo-embedding of biological macromolecules at native conditions more than 30 years ago, techniques and equipment have been drastically improved and the structure of biomolecules can now be studied at near atomic resolution by cryo-electron microscopy (cryo-EM) while capturing multiple dynamic states. Here we review the recent progress in cryo-EM for structural studies of dynamic biological macromolecules.

Scope of review: We provide an overview of the cryo-EM method and introduce contemporary studies to investigate biomolecular structure and dynamics, including examples from the recent literature.

Major conclusions: Cryo-EM is a powerful tool for the investigation of biological macromolecular structures including analysis of their dynamics by using advanced image-processing algorithms. The method has become even more widely applicable with present-day single particle analysis and electron tomography.

General significance: The cryo-EM method can be used to determine the three-dimensional structure of biomacromolecules in near native condition at close to atomic resolution, and has the potential to reveal conformations of dynamic molecular complexes. This article is part of a Special Issue entitled "Biophysical Exploration of Dynamical Ordering of Biomolecular Systems" edited by Dr. Koichi Kato.

1. Introduction

Modern cryo-electron microscopy (cryo-EM) began with the introduction of a unique specimen preparation method by Dubochet and coworkers in the 1980s [1,2], resulting in the preservation of biological specimens at near native condition within a thin amorphous ice film, which allowed direct observation on a low dose transmission electron microscope operating at liquid nitrogen temperature or below. It has become one of the most powerful tools to solve the structure of biomolecules at near-atomic resolution, accompanied by X-ray crystallography and nuclear magnetic resonance (NMR) spectroscopy. With the cryo-EM method, which does not require three-dimensional (3D) crystals, organic macromolecules can be observed directly in multiple conformations in their native environment. This makes analysis more challenging but provides for a richer insight into the dynamic behavior of these biological entities.

Cryo-EM can be used for structure determination of isolated biomolecular complexes across a wide molecular mass range from proteins with several tens kilo-Daltons to virus particles with many mega-Daltons (Fig. 1) and to whole cells. Unlike X-ray crystallography and NMR spectroscopy, cryo-EM requires a much smaller amount of sample and it accepts a larger variation of specimen types, such as single protein molecules, large protein complexes, thin-protein crystals, virus particles, helical fiber complexes, bacteria, cells and even entire tissue sections. The maximum observable object size is essentially only limited by the specimen thickness that can be penetrated with the electron beam, which depends on the mean free path and is approximately 500 nm in the case of 300 kV transmission electron microscopes (TEMs). In the case of eukaryotic cells, observation areas may be limited to the periphery of the cell body or it may be necessary to thin the sample before observation by cryo-sectioning or FIB-milling.

The lower molecular weight limitation is a challenge for cryoEM at present. It is expected around 38 kDa calculated from estimates of the SNR for such proteins under consideration of the limiting dose rate [3]. The minimum detectable size of isolated biomolecules is restricted by the image contrast generated with the specimen-tolerated electron dose. The permissible electron dose is limited by radiation damage to the specimen, which depends on acceleration voltage and spatial resolution as well as sample properties. It is estimated at less than 20 $e^-/Å^2$ at 200 kV accelerating voltage for near-atomic resolution [4]. Merk

☆ This article is part of a Special Issue entitled "Biophysical Exploration of Dynamical Ordering of Biomolecular Systems" edited by Dr. Koichi Kato.

* Corresponding authors.
E-mail addresses: kazum@nips.ac.jp (K. Murata), matthias.wolf@oist.jp (M. Wolf).

http://dx.doi.org/10.1016/j.bbagen.2017.07.020
Received 3 April 2017; Received in revised form 22 July 2017; Accepted 25 July 2017
Available online 27 July 2017

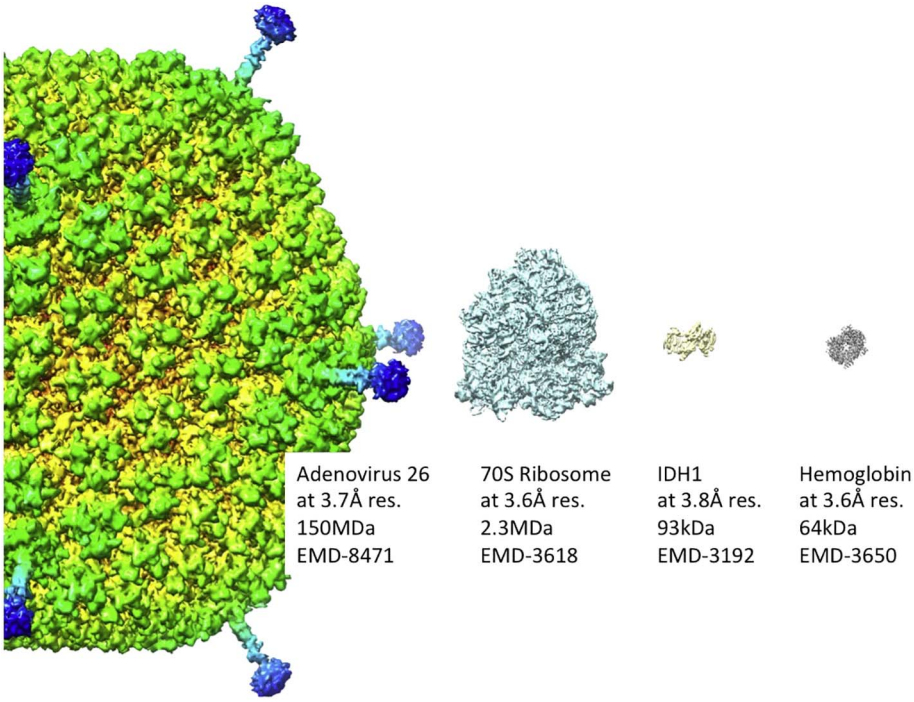

Fig. 1. Representative biomolecules solved by cryoEM at near-atomic resolution. Cryo-EM covers a wide molecular weight range of specimens, from protein complexes in the tens of kilo Daltons to large virus particles with hundreds of mega Daltons. Estimated resolution of the reconstruction, molecular weight and EM data base number are indicated for each particle. From left, species-D human adenovirus 26 [94], 70S ribosome [95], isocitrate dehydrogenase 1 (IDH1) [5], and human hemoglobin [6].

et al. reported the structure of isocitrate dehydrogenase 1 (IDH1; 93-kDa) by single particle cryo-EM at 3.8 Å resolution [5] (Fig. 1). The low signal-to-noise ratio (SNR) due to the small mass giving rise to electron scattering generally hampers identification and error-free alignment of such particles in low dose images. However, at present routine structure resolution of such small molecules is not the norm. Khoshouei et al. analyzed the structure of the 64-kDa human hemoglobin particle at 3.2 Å resolution by contrast-enhanced cryo-EM using a Volta phase plate (VPP) [6] (Fig. 1). The lower limit of molecular weight accessible by cryo-EM has now been extended towards the upper molecular weight range of NMR, which lies around 50 kDa.

Cryo-EM is a suitable technique for visualizing radiation-sensitive specimen like biological macromolecules or soft matter materials consisting of light atoms such as organic polymers. In general, biological molecules form an intact structure in fully hydrated or in partly hydrated form (e.g. when embedded in a lipid membrane) and generally perform their function with large areas of their surface exposed to aqueous environment. This predestines cryo-EM as a tool to observe such structures in their near-native environment. In the cryo-EM procedure, specimens are created by rapid freezing of biomolecules in solution and loaded into the column of an electron microscope operating at high-vacuum and at low temperature to keep the ice in amorphous state and to reduce the effect of radiation damage [7]. Ice can exist in various temperature-dependent modifications – chiefly, in cubic (− 123 °C to − 148 °C, 115 to 150 K) and in hexagonal crystal form (above − 103 °C, 170 K) [8]. During rapid freezing, the formation of these crystalline phases is bypassed to form amorphous ice, but the sample must be kept at a temperature below the crystalline transition temperature. Although specimen embedding in amorphous ice is most commonly used today, cryo-EM of tobacco mosaic virus has been carried out in cubic ice and the conclusion was that better images could be obtained than in amorphous ice [9]. In the past, imaging of two-dimensional crystals at liquid helium temperature (− 269 °C, 4 K) has been successfully used [7,10] with the aim to reduce radiation damage even further. The underlying hypothesis is that ionizing radiation leads to secondary chemical reactions and a “cage effect”, which slow displacement of molecular fragments and that their diffusion rate is governed by temperature [11]. Liquid nitrogen was found to provide the most consistent data quality at near-equivalent damage protection than at lower temperature [12]. Intermediate temperature between liquid nitrogen and liquid helium may change electronic properties of ice (e.g. conductivity) and hence reduce other image-degrading effects such as specimen charging [13,14]. However, the technical requirements and experimental complexity are much reduced at liquid nitrogen temperature (− 193 °C, 80 K), which has become the most commonly used condition for cryo-EM imaging.

Recent advances of cryo-EM are provided by two major innovations. One is the employment of direct electron detector (DED) for electron microscopy. DED can detect electrons directly and read them at high frame rate without a mechanical shutter. Their higher performance is due to greatly improved quantum efficiency as compared to previous generations of detectors. Motion correction has become the standard to compensate for the blurring effect of stage drift and beam-induced movement [15,16]. The other is advancement of image processing methods and the constant increase of microprocessor performance, which allow accurate classification of hundreds of thousands of EM images with computationally expensive algorithms. These two technologies have led to a “resolution revolution” with atomic structures no longer being the exclusive prerogative of x-ray crystallography or NMR spectroscopy [17], and cryo-EM becomes a tool to be able to analyze the structure of dynamical biomolecules.

Fig. 2 illustrates the workflow of cryo-EM. The upper and lower non-labeled area is common in all types of cryo-EM, which includes sample preparation, low dose data acquisition, and model building. The middle blue-labeled area includes two modalities for 3D data acquisition and reconstruction, single particle analysis (SPA), and sub-tomogram averaging (STA). Here we review the basic procedures, the two modalities, and model building including recent advances in cryo-EM for structural studies of dynamic biological macromolecules.

2. Sample preparation and image acquisition for cryo-EM

2.1. Sample vitrification for cryo-EM

Macromolecules in solution are typically applied to a holey carbon film covering a special EM grid (Fig. 3). These commercially available mesh grids are made of a variety of conductive materials (copper, gold, molybdenum, silicon nitride, silicon oxide, and others) and are covered

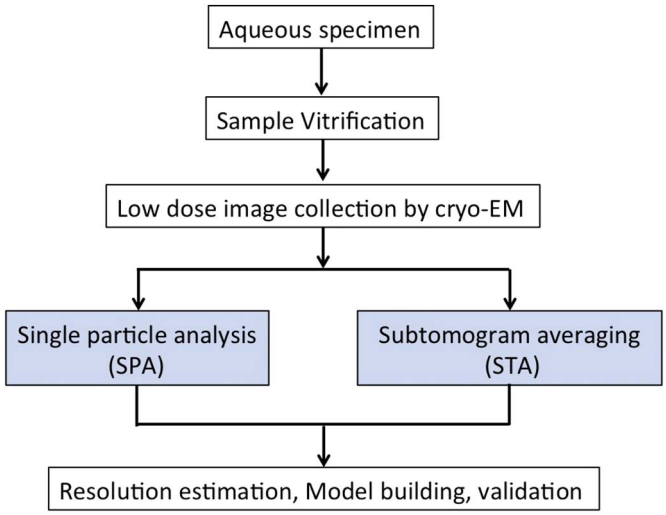

Fig. 2. Cryo-EM workflow. Protein particles in aqueous solution are typically vitrified in amorphous ice by plunge-freezing. Thick objects like large cells or tissue samples require high-pressure freezing followed by cryo-sectioning or cryo-milling. Their images are recorded as projections in the electron microscope at low temperature using low electron dose to avoid radiation damage. Fundamentally, two related modalities (blue boxes) are used - single particle analysis (SPA) and cryo tomography, which is often followed by subtomogram averaging (STA). If quality and resolution of the reconstructed electron potential map ("the structure") allow, an atomic model can be built and refined using known chemical constraints.

with a perforated support film (usually a 10–50 nm thin carbon film, a 5–10 nm thin gold film, or thin films of various thickness made from silicon derivate) with regular hole arrays of defined shape, size and pitch (e.g. Quantifoil (Quantifoil Micro Tools), or C-flat (Protochips Inc.)). 2 to 3 ml of hydrated specimen is applied onto the perforated grid, which is pre-treated by glow discharging. After removing excessive solution with filter paper under tightly controlled environmental conditions, the grid is plunged rapidly into a cryogen, which is generally precooled with liquid nitrogen (Fig. 3).

Depending on the molecular adhesion properties of the sample particles, the surface of this support film must be pre-treated before sample application to produce an even particle distribution. For most soluble samples, this requires a hydrophilic surface, which can be created with ion bombardment in a glow-discharging device or by plasma cleaning (essentially, glow discharging in the presence of a gas or a gas mixture like hydrogen/oxygen). The latter can also remove undesirable hydrophobic organic contaminants (e.g. carbohydrates precipitated from the atmosphere during grid storage or transport). While these methods typically result in a predominantly negative surface charge, additives such as polyethyleneimine or polylysine create a positive surface charge [18]. Variation of these parameters may be used to influence particle orientations or to drive particles into holes for higher local concentration. In the case that a hydrophobic surface is desired (e.g. for lipid-embedded two-dimensional crystals or certain cell types), additives like amylamine can be added to the evaporation chamber [19]. However, this tends to contaminate a glow-discharging chamber permanently and a dedicated device is recommended. In addition, Kelly et al. have introduced surface-modified "affinity grids", which feature a lipid monolayer film with functionalized head-groups that can capture and orient particles with high specific binding affinity for efficient on-grid purification from ultra-low particle concentrations [20]. Their disadvantage consists in additional background from the affinity support film.

The most common cryogen is liquid ethane. A mix of ethane and propane was found easier to use than ethane with plunge freezing devices that do not control the cryogen temperature. The advantage of using an ethane-propane mix over pure ethane is its reduced freezing temperature, which allows direct thermal contact between liquid nitrogen and the cryogen without freezing of the mixture. In contrast, pure ethane does freeze at liquid nitrogen temperature and requires constant thawing and re-cooling [21]. The frozen grid is then preserved in liquid nitrogen storage until use. Since its inception, the method has become a standard sample preparation method for cryo-EM. At present, ice embedding of specimens can be done reproducibly with a blotting robot (e.g. FEI Vitrobot, Leica EM GP, or Gatan CP3), which removes excess liquid by wicking action with a filter paper while controlling multiple environmental parameters like blotting time and blot force in addition to temperature and humidity. The procedure requires only a few microliters of protein solution at moderate concentration (0.1–2.0 mg/ml, depending on molecular weight).

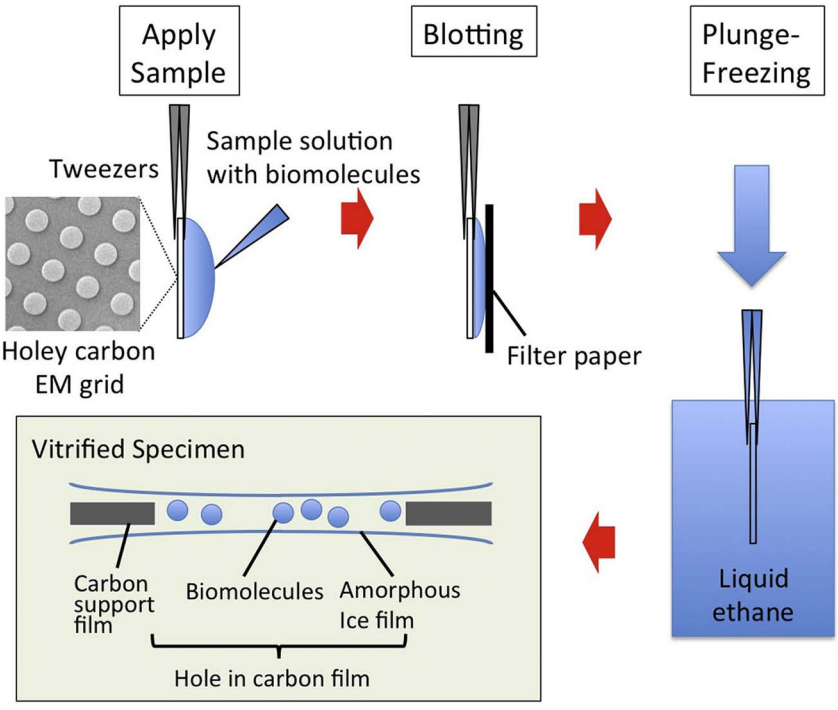

Fig. 3. "Classic" specimen preparation by plunge-freezing. Aqueous sample solution is applied onto glow-discharged (hydrophilic) holey carbon film supported by EM grid. Excess solution is removed with filter paper from one or both sides. Blotted grid is rapidly plunged into a cryogen precooled at liquid nitrogen temperature. Biomolecules embedded in thin amorphous ice film are observed in cryo-electron microscope.

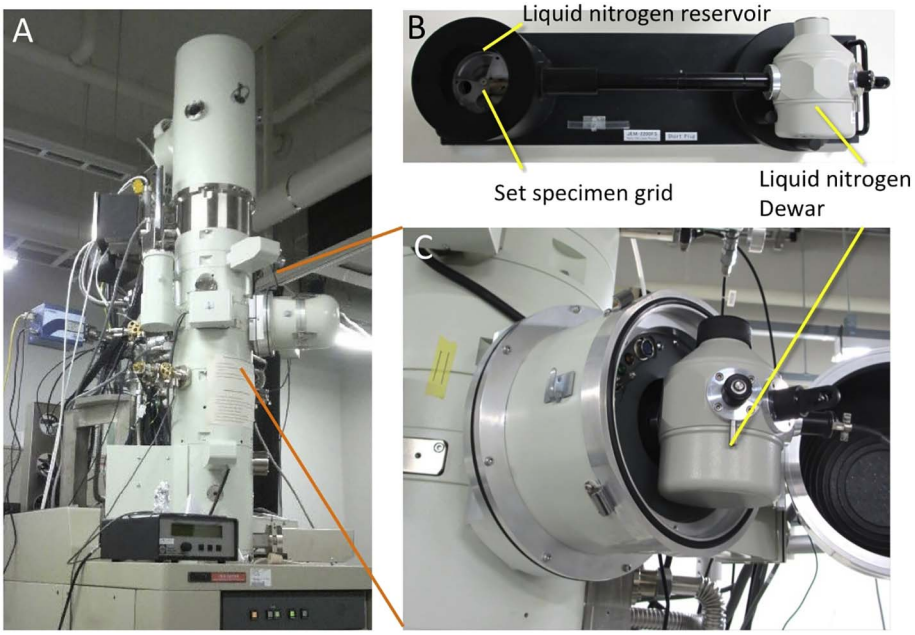

Fig. 4. Representative cryo-EM equipment. A) Electron microscope using 200 kV field emission electron source (JEOL 2200FS). B) Side-entry type cryo-transfer specimen holder (Gatan 626). C) Frozen grid is mounted on a cryo-transfer holder and inserted into the EM column without ice-contamination.

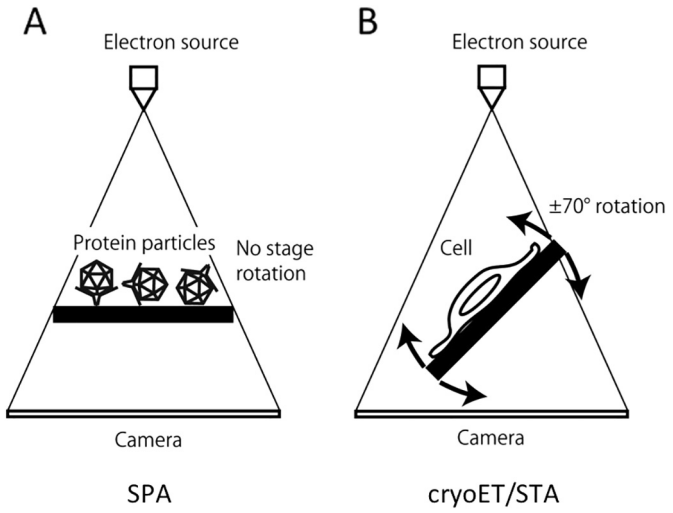

Fig. 5. Data acquisition procedures for two modalities. A) For single particle analysis (SPA) the images of randomly orientated homogeneous particles are recorded at low electron exposure (dose). Then, particle images selected from digitized images are iteratively aligned against a reference and averaged. B) Electron tomography for sub-tomogram averaging (STA). 2D projections of heterogeneous particles are collected by tilting the specimen stage, and 3D tomograms are calculated using weighted back-projection or other reconstruction algorithms. Selected subsets of the tomogram ("sub-tomograms") containing individual particle volumes are picked, aligned, classified and averaged.

Even semi-automated plunge-freezing with robotic assistance is still a labor-intensive process and requires a skilled operator. Sample preparation for cryo-EM in the age of high throughput image acquisition is therefore steadily becoming a limiting factor, which has been recognized within the community. Multiple new approaches to cryo-embedding are currently under active investigation and development [22,23].

2.2. Low dose image collection

High-resolution cryo-EM images of ice-embedded biomolecules on holey carbon EM grids are taken using low dose procedures to avoid irradiation damage and are recorded on a digital detector or on photographic film. The frozen grid is mounted on a cryo-transfer holder equipped with liquid nitrogen Dewar in a cryo-workstation to avoid ice contamination (Fig. 4). Then, the ice-embedded specimen is loaded in frozen state contamination-free into the cryo electron microscope by means of a cryo-transfer holder. Some high-end electron microscopes, which are dedicated specifically for cryo-EM use, have specially designed cryo-specimen cassettes for holding a dozen of frozen cartridge-mounted grids simultaneously within a microscope-attached autoloader (e.g. FEI Titan Krios, FEI Talos Arctica, JEOL CryoARM). With general side-entry cryo-transfer holders, the stage usually stabilizes within tens of minutes after loading the holder into the column. Commercially available cryo-EM grids contain a regularly spaced uniform hole pattern edged into a thin (10–50 nm) carbon support film. An aqueous film whose thickness accommodates the solubilized macromolecules in a single layer is formed on the holey carbon support film after blotting and preserved as amorphous ice by plunge-freezing (Fig. 3). Images of holes are taken using low dose mode. The low dose mode can minimize irradiation damage to the specimen by navigating to the position of the object at low magnification or in defocused diffraction mode. Focus is adjusted nearby without exposing the target area and then an exposure of the target is acquired at the desired preset magnification.

3. Single particle analysis (SPA)

3.1. Principle of SPA

Structural determination by SPA has developed into a powerful technique rivaling x-ray crystallography for successful determination of biological structures that have eluded crystallization. The principle of SPA is not reconstruction of the structure from a single biological molecule, but averaging multiple views of many copies of the same molecule (Fig. 5A). This is, why SPA is sometimes also referred to as single particle averaging. The underlying assumption is that the three-dimensional objects, which are represented by their two-dimensional projections captured on the image sensor, are identical. Unlike tomography, which records multiple views of the same biological object and thus accumulates the full electron dose of an entire tomographic tilt series onto this radiation-sensitive protein sample, the SPA data collection strategy distributes the electron dose between the many copies of identical biomolecules. Because each molecule is frozen in a random orientation, it is not necessary to tilt the specimen stage for complete

rotational sampling. Without the need for multiple exposures due to specimen tilting, the maximum electron dose tolerated before significant radiation damage sets in, is 1–2 orders of magnitude higher for an SPA exposure than what is acceptable for a single tomographic tilt frame. In addition, typical SPA datasets consist of thousands of images, each of which contains up to a thousand projections of the biological molecule in different orientations. When identical views of the same object are summed up, the SNR of the resulting averaged projection increases dramatically, because the small pixel intensity variations caused by the scattering from the protein object during its exposure to the electron beam add up coherently, whereas noise is distributed randomly (it still follows a distribution) and this tends to get suppressed by averaging.

The typical image reconstruction workflow alternates between two steps: orientation search for all projections and 3D reconstruction, in which all aligned projections are accumulated in a 3D-array, resulting in a 3D electron potential map. This cycle is usually iterated until the resolution does not improve further.

3.2. Image processing for SPA

Cryo-EM images are usually collected in defocused condition for increased phase contrast. These images are modulated in frequency space by the phase CTF (Contrast Transfer Function). Image CTF must be estimated for later deconvolution. Currently, several software for CTF estimation is available (e.g. ctffind [24], gctf [25], e2ctf.py [26]). Particle positions must be selected from the micrographs. After the CTF estimation, particle images randomly oriented are collected. Several correlation-based automatic particle picking programs are available at present, (e.g. e2boxer.py [27], Relion-autopick [28], Scipion [29], FindEM [30], Signature [31]). Particle images recorded in different orientations are aligned and classified.

The largest impact on mainstream improvement of results was probably due to making ML (Maximum likelihood)-based 2D and 3D classification including Bayesian statistics practically feasible by clever implementation on today's computer hardware. While earlier work was indispensable to point the way [32], only later algorithms were optimized enough for practical use (Frealign [33], Relion [28], EMAN2 [27], Frealing/cisTEM [34], Spire [35], and cryoSPARC [36]). But the largest attraction for novel users can likely be attributed to a user-friendly implementation by introducing an easy to use graphical user interface. These programs now cover the entire workflow from motion correction, automatic particle selection, 2D image classification, image browsers with various statistical parameters, to 3D reconstruction and classification.

3.3. 3D reconstruction of the structure

In the classic workflow, classified images are used for 3D reconstruction by means of a back-projection algorithm after determining their orientations [37]. Prior classification increases the SNR, but reduces the dataset to a discrete number of classes with limited resolution. The initial 3D map is iteratively refined with a projection matching procedure. Modern packages can operate on individual projections. The principle of 3D reconstruction from 2D projections is the central section theorem [38,39], which states that the 2D Fourier transforms of the projections of the same 3D object lie on planes centered at the origin of the 3D transform of the object. At the time of insertion of the 2D transform into the 3D array (or sometimes before), a correction for the point spread function of the defocused image is applied. This is referred to as correction for the CTF of the optical system of the microscope. It is an operation essential for restoration of high-resolution information, which is shifted radially outwards and accompanied by periodic phase shifts as in an Airy disk of a point source, and it is accomplished by deconvolution of the defocused image with the previously fitted phase CTF of the microscope. This phase-corrected image is often scaled, weighted and treated with a band-pass filter before its insertion into the 3D array. While not all reconstruction methods are Fourier based, the procedures are mathematically equivalent. Fourier methods, however, are often easier to implement and very similar to methods used for reconstruction of diffraction images. After all, the Fourier transform of the image of a thin phase object, which is the result of interference of arrays scattered by the object and the unscattered beam after their recombination by the objective lens is proportional to the diffraction pattern recorded in the optical diffraction plane: the intensities measured in the diffraction spots of crystallographic data are the squares of the amplitudes and are equivalent to spots in the Fourier transform of an electron micrograph. But aren't there no spots in the image transform of a non-crystalline sample without periodicity? While this is correct, it does not matter for the purpose of 3D reconstruction, since the transform of a non-periodic object is continuous, but sampled at pixel interval. The fact that it is pre-aligned against a 3D reference omits indexing. The back-transform of the symmetrized 3D Fourier array to the resulting normalized 3D map represents the reconstructed electron potential. When visualized at an appropriate contour level (e.g. at 3 standard deviations above average, or “3 sigma”) and of sufficiently high resolution, it allows building of an atomic model by placing atomic coordinates into the map. This process can be partly automated if the quality of the map is very high. The process involves incorporation of constraints imposed by knowledge of chemical properties like bond lengths and peptide geometry.

4. Subtomogram averaging (STA)

4.1. Principle and practice

A recent successful development in tomography is subtomogram averaging. While “classic” SPA relies on alignment, averaging and 3D reconstruction from 2D projections, STA starts from tomograms of nearly identical 3D structures frozen in vitreous ice. The process begins with data collection by tilt series followed by tomographic reconstruction (Fig. 5B). Before STA, one of the disadvantages of conventional tomography based on tilt series was known as the “missing wedge effect”. Since a typical sample holder cannot be tilted by more than ± 70 degrees, there is a direction perpendicular to the beam, which does not contain any views of the object. In reciprocal space, this can be visualized as a missing wedge of data. It manifests itself in anisotropic resolution of the tomographic reconstruction, with some features entirely absent when viewed from the direction of the missing data. Dual axis tilt acquisition strategies, in which the sample is rotated by 90° in plane before another tilt series is started, can significantly reduce this effect to a “missing pyramid” of data [40], or even to a missing cone [41]. However, the dose must either be increased to accommodate the additional images, which increases damage. Or the tilt step interval must be made coarser while keeping the dose constant, thereby increasing noise. In practice, single tilt tomography has remained the most commonly used technique despite the missing wedge artifacts. Modern tilt data collection can be optimized for efficient “dose-symmetric” [42] acquisition strategies, or follow the classic single axis tilt data collection scheme. In all cases, which aim for following up by averaging methods, a greater emphasis lies on the first frames, which have experienced the least amount of radiation damage. From the reconstructed tomogram, multiple copies of the particles are selected and boxed as volumes, resulting in a stack of already reconstructed 3D particles, or “subtomograms” (instead of a stack of 2D projections as in SPA). If the sample distribution (i.e. random orientation of identical particles) and available beam time allow the collection of a larger number of reconstructed subtomograms, STA can result in increased SNR of the final subtomogram average and simultaneous reduction of missing wedge artifacts, because particles are randomly oriented with respect to the beam. In addition, because the location of

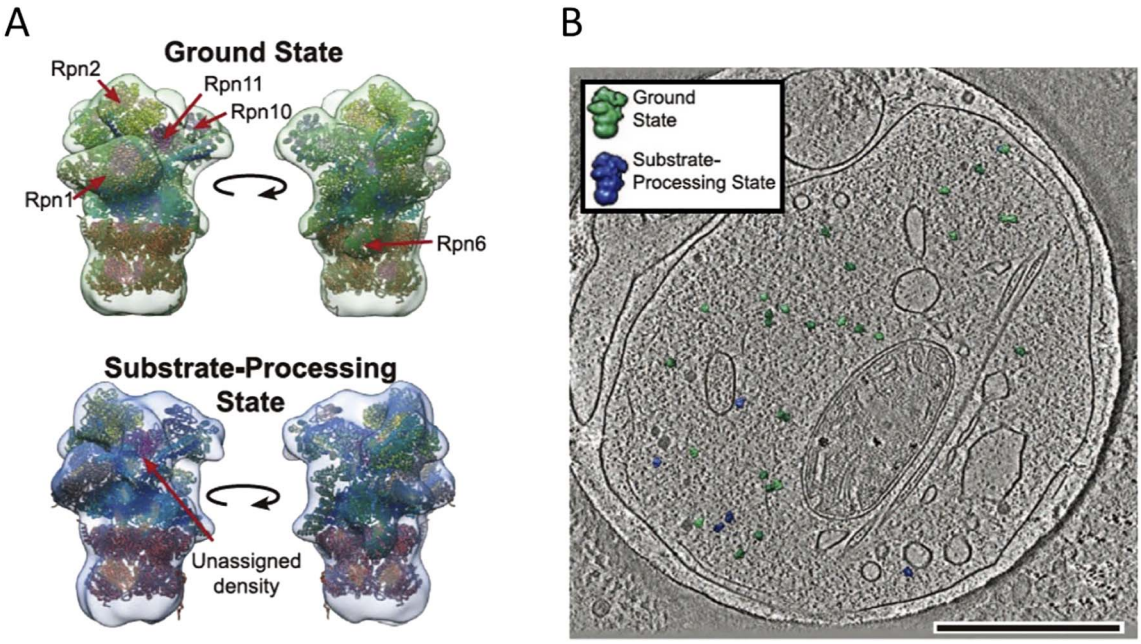

Fig. 6. Contrast-enhanced cryo-electron tomography with Volta phase plate shows dynamic states of 26S proteasome in their functional and unperturbed cellular environment (in situ). A) Mammalian 26S proteasome subunits after sub-tomogram averaging and 3D classification with fitted atomic models (from *S. cerevisiae*) in two biologically significant states. B) One tomogram slices through an annotated 3D atlas of a cell with individual orientations and conformational states of 26S proteasomes. Colored isosurfaces from (A) are overlaid. In the absence of proteotoxic stress, only 20% of 26S proteasomes in this molecular census of the entire cell were found to be in the substrate processing state (blue), suggesting that in the absence of stress their capacity is not fully used. Scale bar, 500 nm. (Reproduced from [46] with permission).

each subtomogram within the field of each image is known, a more precise CTF correction can be applied to each projection before its reconstruction while also applying a sensible mask to reduce alignment bias by the missing wedge data [43]. This procedure including iterative alignment and reconstruction with individual movie frame processing followed by ML-3D classification is now implemented in the latest version 2 of Relion [44]. A similar workflow has also been described by Briggs et al., leading to the currently highest subtomogram averaging of a viral coat protein of HIV at 3.9 Å resolution [45].

4.2. Advantage of STA

When it becomes difficult or impossible to recognize individual particles easily – e.g., against the noisy background of a cell, there is no alternative to tomography. The power of modern STA is illustrated in a landmark study by Asano et al., who were able to extract, average and 3D-classify subtomograms of multiple forms of the proteasome in situ inside a thin-sectioned cell, at nanometer resolution (Fig. 6) [46]. Ultimately, their third dimension is an advantage of subtomograms over the 2D projections used in SPA, because the absolute handedness of a structure is lost in projection. This loss of information can lead to ambiguities about which side is facing up or down. While this statement may appear trivial, history has shown that many structures have been reconstructed incorrectly due to the lack of 3D information [47]. STA can overcome this problem while retaining the ability to reach high resolution. A clever way to determine absolute handedness with limited amount of effort was introduced by Briegel et al. [48] by adding a unique fiducial with known hand. In addition, STA is applicable to entirely novel structures with unknown symmetry or difficult cases with high conformational flexibility (e.g. motor proteins like myosin or dynein) and may result in a correct set of 3D conformations, whereas an incorrect alignment reference may trick the SPA method towards a biased result despite proper classification. The drawback, however, is much lower throughput due to tilt series acquisition and technical challenges for extremely precise stage control, tracking and CTF correction. Once these are overcome – e.g. by adding fast continuous tomography acquisition at movie rate on a direct electron detector [49] – and corresponding additional improvements in tomography software – there should not remain much difference between the results achievable by SPA and STA. Together with novel methods in NMR spectroscopy which can describe the full conformational range of a structure [50], cryo-EM will become a technique of choice for analysis of flexible molecules. The future looks bright indeed for structure determination of dynamic structures.

5. Resolution estimation, model building and validation

Resolution of the reconstruction is generally estimated by comparing two reconstructions each from a half set of images (e.g. all even numbered particle images, and all odd numbered images) in the frequency domain, i.e. after Fourier transformation of the volume. Due to their different data content, the two half set reconstructions begin to differ more and more as the level of detail (the spatial frequency) increases. This correlation coefficient is plotted as the Fourier shell correlation (FSC). If the alignment algorithm took care to minimize reference bias, a threshold at FSC = 0.5 was originally used to indicate the resolution of the map [51]. Rosenthal and Henderson [52] introduced a lower threshold at FSC = 0.143 based on the fact, that the resolution of the final reconstruction is higher than its half-sets used for FSC. This value is consistent with criteria used in x-ray crystallography. It has been argued that no fixed value should be used - in particular when symmetry is applied to both half set reconstructions ("half bit" criterion, [51]). In an attempt to further reduce possible reference bias, resolution measurement after fully independent refinement and reconstruction is referred to as the "gold standard FSC" [52]. However, when identical starting 3D references have been used for both refinement runs from the beginning, such reference bias is not avoided and the advantage of the gold standard method becomes questionable. In any case, the FSC measures similarity between two data sets and is only an indicator for the resolution of the reconstruction, but no validation. For tomography data, care must be taken not to bias the resolution measurement by the presence of edge effects in reciprocal space caused by the missing wedge of data. This is usually accomplished by substituting missing values with average density values. The problem is

much reduced after STA. While the measured value for map resolution is not a form of validation, it is an important parameter, which must be reported with each deposition. It has become standard practice to document the quality of a map by computed color-coded "local" resolution values, which indicate resolution anisotropy in the real space reconstruction (e.g. Resmap [53], Blocres [54]).

The final purpose is to understand the molecular structure and the structural dynamics in the biomolecules. Once a high-resolution structure has been reconstructed beyond 4 Å, it is often possible to build an atomic model of the entire molecule de novo, or by rigid-body docking or fitting of existing model coordinates. The preferred workflow depends on map resolution and typically alters between manual building (e.g. Coot [55], O [56]) and automated refinement (e.g. refmac [57], phenix_real_space_refine [58]) by incorporating chemical knowledge and force fields. Most of these programs operate on real space maps. Under favorable conditions and in particular if symmetry can be exploited, it is sometimes possible to generate model sets fully automatically (e.g. rosetta [59]). At low resolution (less than 4–6 Å), methods, which incorporate additional physicochemical constraints like molecular dynamics [60] or normal mode analysis [61], are required. A refined model must be validated with crystallographic geometry validation tools, which produce a variety of statistics and check for stereochemical outliers of the atomic coordinates. It has become common standard and it is now prerequisite to deposit maps in public databases (e.g. Electron Microscopy Data Bank EMDB) together with model coordinates (RCSB Protein Data Bank PDB).

6. Advanced techniques

For the current advancement of cryo-EM for structural studies of biomolecules and biomolecular dynamics, a lot of innovations have been adopted. In this section, we introduce these prerequisite technologies.

6.1. Direct electron detectors and "movie mode"

The great success of SPA in the past ten years is chiefly based on concerted improvements in detectors, instrumentation and software. Direct electron detectors (DED) or direct detection devices (DDD) based on radiation-hardened CMOS technology derived from high energy physics, and lessons learned from x-ray synchrotron detectors have ushered in a new area of nearly noise-free image sensors with high detective quantum efficiency (DQE). They have entirely replaced plate cameras based on photographic sheet film coated with an electron-sensitive silver halide emulsion as well as the previous generation of scintillator-coupled CCD detectors. All DDDs can operate at moderate (20–40 frames per second, e.g. FEI Falcon 2, Direct Electron DE-20 and DE-64) to high frame rates (400–8000 fps, e.g. Gatan K2, Gatan K2-IS, PNDetector pnCCD). These make a possible to perform motion correction of the image frames and high-resolution imaging [62].

Their operation in "movie mode" allows compensation of residual stage motion as well as motion of the image due to beam-induced charging. Software, which can perform such motion correction, relies on averaging after frame alignment and may be used on-the-fly with appropriate hardware (e.g. FEI Falcon3EC processor) or a dedicated powerful computer (Appion [63], FOCUS [64]). Geometric distortions caused by the projector lens system can be measured and corrected (unblur [15]). It has become common practice to use a dose-dependent filter, which weights the amplitudes of each movie frame in the frequency domain in order to retain strong low resolution contrast while retaining high resolution information from early frames which have suffered less from radiation damage (e.g. motioncor [16], motioncor2 [65], unblur [15], Direct detector utilities [66]). Single electron counting and super-resolution interpolation have become practical in real-time operation implemented on dedicated field programmable gate arrays (FPGAs) (e.g. Gatan K2 Summit, FEI Falcon 3EC). 2 × super-resolution interpolation results in a 4 × larger pixel count of the output image with signal detectable beyond the Nyquist limit of the physical pixel array (Gatan K2 Summit). The advantages are slightly improved DQE performance after down sampling by Fourier cropping, which eliminates additional noise in the form of aliasing effects, or a wider field of view. The latter is also achieved by a native 8 k × 8 k pixel sensor (Direct Electron DE-64), which has the benefit of higher throughput by capturing 4 × the area and proportionally more single particle images compared to a 4 k × 4 k sensor.

6.2. Phase contrast and phase plates

Contrast formation in the TEM is a combination of amplitude contrast, which is chiefly due to inelastic interaction of the beam with the sample, and phase contrast, which is strongly modulated by the phase CTF of the optical system of the microscope. Since the fraction of amplitude contrast at typical energies of modern TEMs (120–300 keV) is only 5–10%, images are usually recorded at defocused condition to gain phase contrast, and the frequency-dependent displacement of the radially shifted point spread is later restored by deconvolution with the experimentally determined phase CTF. However, the defocus-induced blurring of the observed object features makes direct interpretation difficult and attenuates high resolution information with increasing defocus due to limited coherence and aberrations.

The image in the TEM is formed by interference between the unscattered electron wave, which has never interacted with the thin sample, and the scattered waves whose phases were altered as a result of the interaction with the electric potential of the object. When the scattered and unscattered waves are combined in the image plane, an image with varying brightness arises and its features are due to these subtle phase differences and the CTF. Thus, image formation in the TEM is sometimes referred to as "in-line holography". More than 60 years ago, the Dutch physicist Fritz Zernike realized that such phase differences could be greatly increased by systematically delaying or accelerating the phase of the scattered wave. He accomplished this by introducing a ring-shaped phase-shifting device – a wave plate, or phase plate – in the back focal plane of an optical light microscope (the optical diffraction plane), which led to his Nobel Prize for the discovery of phase contrast microscopy in 1953 [67]. For the rest of his life, he worked on the practical implementation of his idea for the TEM, but technical difficulties were only overcome by Nagayama et al. with the "Zernike" phase plate, which is a thin phase-shifting carbon film mounted in the back focal plane with a central hole for the central unscattered beam [68]. However, this device also suffered from rapid charge build-up, performance degradation by small contaminants, and the requirement for very precise positioning of the central hole. Only recently, novel types of phase plates have made routine use of this ground-breaking effect in the TEM practical: in particular, the VPP, which is based on a heated continuous carbon film that gets charged up by the unscattered central beam itself, whose phase it shifts [69]. Other electrostatic designs (e.g. Siemens star, Half phase plate, Ampere phase plate) based on precisely shaped external electric potentials are still under development and promise easier image acquisition and data processing procedures due to constant user-controllable phase shift [70].

In theory, an in-focus phase contrast image with a quarter wave phase plate (phase shift = 90°) results in flat high contrast transfer across the frequency spectrum. Such an image represents large and small features at equal contrast and makes it therefore easy for an observer to interpret the imaged structure directly. However, one of the practical difficulties of in-focus phase contrast is accurate focus within 100 nm during automated data collection for SPA. This is due to the fact that commercially available holey carbon foils used as specimen support are not always flat and may wrinkle due to unisotropic contraction upon plunge freezing. Because no Thon rings are visible at such low defocus, CTF estimation is not practical. Despite multi-point off-axis

focusing, it is hard to obtain higher resolution than ~4 Å [69]. Deviations as small as 200 nm from true focus introduce strong oscillations of the phase CTF in the high frequency part of the spectrum and deteriorate the signal at high resolution upon averaging. An alternative to in-focus phase plate imaging is defocused phase plate imaging, which results in visible Thon rings in the image power spectrum that can be used for fitting and deconvolution of the phase CTF including astigmatism and phase plate-induced phase shift. With this method, very high resolution better than 3 Å has been achieved [71] and a small protein of 64 kDa molecular mass has been resolved to 3.2 Å resolution [6] using SPA with VPP. Nevertheless, accurate estimation of the variable charge-induced phase shift of a VPP is still challenging and requires stringent selection of outliers from the expected phase shift curve evolution.

Phase contrast imaging with contrast-inducing phase plates holds the promise of obtaining high resolution reconstructions with a smaller amount of particle images, because the enhanced contrast facilitates particle alignment and classification. For dynamic structures, whose images must be sorted into discrete classes, this represents a clear advantage. The same should apply to phase plate tomography and STA. In summary, the use of a phase plate device for contrast enhancement is a small step forward by itself, but in combination with other improvements in direct electron detectors, energy filters, sample preparation and the collection of large amounts of data at movie rate, these incremental advances add up and result in better data with higher SNR for much more efficient analysis with modern image processing techniques.

6.3. Energy filters

Energy filters enhance contrast by filtering out the detrimental contributions of out-of-phase inelastically and multiply scattered electrons. An energy filter in the EM acts like an optical prism – when the electron beam is bent around a tight corner, it is fanned out according to its energy spectrum (thus, its wavelength). Using a mechanical slit of variable width, images can be filtered according to energy range and offset selected by the optical system of the spectrometer and the slit width. For biological applications, typically only the zero-loss filtered image is used (corresponding to elastic scattering events without energy loss). Two types of energy filter are utilized – one is in-column and the other is the bottom mount type [72]. Compared to the in-column energy filter (omega-type and gamma-type), which has a symmetric optical design, the bottom mount filter was more prone to image distortion because of its asymmetrical design. It has, however, been upgraded to minimize geometric distortions to less than 0.5% RMSD across the field of view (Gatan Quantum GIF), which benefits the averaging of large single particle objects like giant viruses and cellular tomography [73]. The combination of energy filter and direct electron detector combines both contrast enhancing effects (e.g. Gatan K2 Quantum).

6.4. Advances in electron microscopes, automation and data handling

On the microscope side, the most significant improvements were multi specimen autoloaders, which allow cryo-samples to be kept for up to 5 days in the autoloader without contamination, upgraded optics by adding a third condenser lens (FEI Titan) for ease of achieving parallel illumination, high coherence Schottky-type or cold field emission emitters (JEOL cryoARM), improved specimen stage stability by eliminating the side entry holder and by fully containing the specimen cartridge inside the microscope column, contrast-improving phase plates, and finally full remote control capability of all microscope functions including aperture control, which eliminates any temperature variations or vibrations induced by a human operator.

This remote-control capability has enabled a new generation of software, which allows fully automated data collection on a well-maintained and calibrated cryo-TEM (e.g. Leginon [74], SerialEM [75], FEI EPU/Tomography4, UCSF-Image4 [76], Gatan Latitude, JEOL JADAS) and results in large amounts of data (typically between 3 and ~ 10 TB of movie data per each sample dataset). Such large datasets must be stored on local redundant arrays of disks (RAID), on storage area networks (SANs) or network-attached storage (NAS) and be processed on computer clusters, which typically have several thousand CPU cores. As in other fields of applied high performance computing (HPC), graphics processing units (GPUs) have been used to accelerate numerically intensive highly parallel computations – for cryo-EM, GPU processing has become popular for motion correction of movie frames (e.g. motioncor1/2) [16,65] and the entire image processing workflow (Frealign-GPU [77], Relion2 [44]) by using cheap “gaming” cards, multiples of which can reach the performance of 100–1000 CPUs in a single chassis under the desk, thereby eliminating the need for a centrally maintained datacenter and saving energy.

In the case of cryo-ET, the specimen holder is rotated at the object and a tilt series of the specimen is collected with continuous or variable tilt angle increment. Modern software for automated image acquisition can create a tiled “atlas” of the entire grid at low magnification, which is then followed by imaging of squares used for indexing of hole positions. Each hole is sequentially targeted for precise adjustment of the stage and multiple exposures can be taken by using image shift after offset focusing, thereby maximizing throughput (e.g. EPU (FEI Company), Leginon [74], SerialEM [75], UCSF Image4 [76], Gatan Digital Micrograph Latitude (Gatan Inc.), Tomography4 (FEI Company)). Such systems allow the collection of up to 3000 single particle images per day and can easily generate more than 3–10 TB of data volume during this time, depending on the number of stored movie frames. Actual throughput depends on many parameters including number of movie frames, network and data storage speed. Current data collection strategies for tomography are much more time consuming (e.g. dose symmetric strategy [42]) and limit the amount of tomograms to about 10 per day. This might be improved by future continuous acquisition tilt tomography, during which a tomogram is collected as a single continuous movie. Indeed, in the field of material science, such continuous acquisition of a low dose tilt series consisting of 3487 movie frames at a frame rate of 1000 frames per second has been demonstrated in only 3.5 s [49]. Adapting this technology for biological samples will enable data collection for subtomogram averaging at a throughput comparable to today's single particle method. While most labs are currently using TEM, cryo-scanning transmission EM (cryo-STEM) has strong potential and has been successfully applied to cellular tomography of thick samples [78].

7. Observation of molecular dynamics

For single particle analysis, the objects must be homogeneous and equally dispersed in a thin ice film, because a prerequisite of the reconstruction algorithm is that particle images represent a series of different projections from identical particles. However, recent software using sophisticated algorithms for 3D classification can separate small conformational changes in single molecules images [79]. Heterogeneous particles have been successfully separated using both SPA and cryo-ET/STA. These breakthrough improvements cannot be overstated, since most recent results showing 3D classes of the particle population prove that the assumption that all particle images are projection from the identical 3D object is incorrect. The observation that discrete subclasses of molecular structure exist becomes even more pronounced as the resolution of their reconstructions is increasing. Most larger proteins and protein complexes contain flexible domains, which can adopt multiple conformations. This may be the reason why such dynamic structures have often eluded crystallization. To obtain the highest levels of resolution achieved by SPA around 2 Å for biological samples as of today, even images of small proteins showed conformational variability which required sorting into their least variable forms by 3D classification [80,5]. The distribution of their dynamic molecular conformations in snap shots captured by different classes may account for preferred

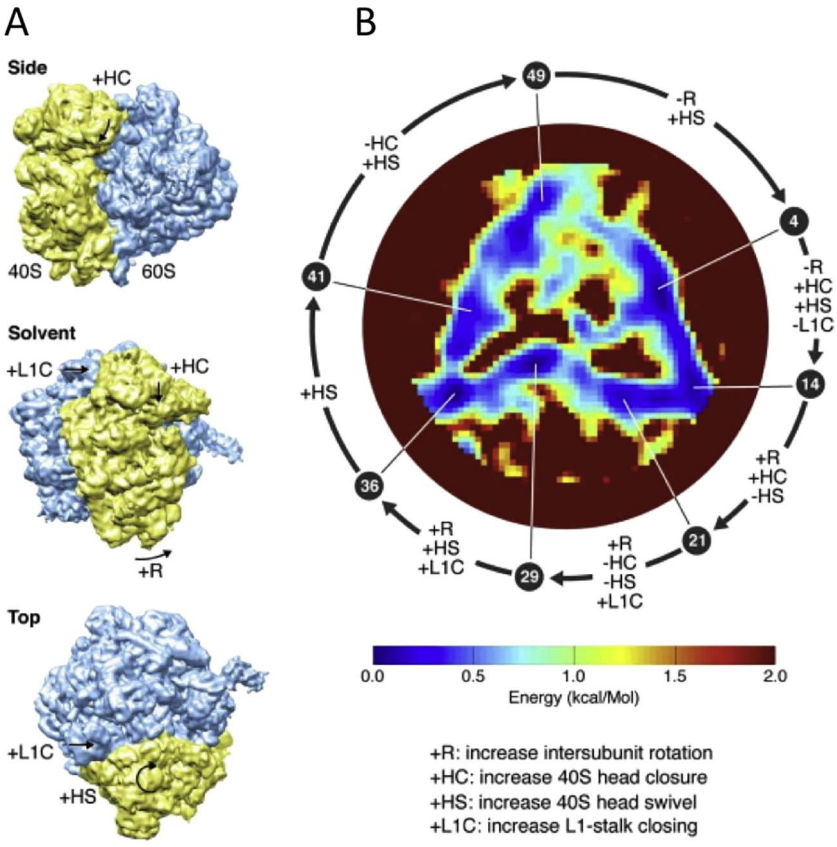

Fig. 7. This work by Dashti et al. correlates conformational states and energy landscape of the ribosome by manifold mapping during 3D-classification. (A) Orthogonal views of a cryo-EM map of the yeast 80S ribosome, with arrows indicating four key conformational changes associated with the elongation work cycle of the ribosome. (B) Energy landscape traversed by the ribosome. The color bar shows the energy scale truncated at 2 kcal/mol to show details of the triangular trough. The arrows indicate the structural changes between 7 selected states, each identified by its place in the sequence of 50 states. (Reproduced from [82] with permission.)

low energy states within a thermodynamic equilibrium and the total population may contain the entire conformational space accessible to the folding of the protein structure under the conditions of its native environment in solution before flash freezing. Indeed, such a quantitative model has been proposed for the dynamic conformational changes of the yeast ribosome based on sophisticated manifold mapping of representative 3D classes (Fig. 7) [81,82]. Such models cannot only unravel the temporal relationship between 3D classes representing different conformations of the structure, but fill in the gaps between transitions of preferred states by assigning them to a multi-dimensional trajectory within a realistic energy landscape and hence explain their mechanism of action by thermodynamic principles. For other examples, Zhao et al. reported the structures of the three rotational states of the yeast V-ATPase by single particle cryo-EM at near atomic resolution [79]. According to the three ATP binding states in cytoplasmic V_1 domain, the whole structure of the multi-complex showed different structures, which were successfully classified at 3D by using Relion [28]. In a recent landmark study, Loveland et al. were able to untangle key states of the ribosome during gene translation, elucidating the mechanism of accurate decoding by ensemble analysis with single particle cryo-EM [83]. As a new tool to study dynamics of membrane proteins, nanodiscs are adapted for cryo-EM SPA. Gao et al. solved the high-resolution structures of TRPV1 ion channels embedded in nanodiscs wit and without ligands and reported that the specific phospholipid interactions enhance binding of a spider toxin to TRPV1 through formation of a tripartite complex. Furthermore, phosphatidylinositol lipids occupy the binding site for capsaicin and other vanilloid ligands and regulate the channel opening [84].

For cryo-ET/STA, it can be used to study molecular states of unique complexes at near-native condition, even though the resolutions are lower than those of SPA [85,86]. Cryo-ET can provide the structure of parts of cells, organelles, and viruses in situ. Liu et al. described structural changes of the envelope glycoproteins of human immunodeficiency virus (HIV) with and without ligand binding to the target cell receptor [87]. The dynamic model of the bacterial type IVa pilus machinery was investigated by cryo-ET/STA by Chang et al. [88], revealing the mechanism of pilus assembly and retraction. CryoET/STA also helped elucidate the dynamics in bacterial chemotaxis [89,90], and bacteriophage infection [91–93], where the dynamical conformation changes of the protein complexes cause the biological functions.

8. Conclusion/perspectives

Here, we give a review of cryo-EM and introduce the technique as one of the modalities for studying molecular dynamics in proteins and protein complexes. Recent advances in hardware and software technology described in this review allow investigation of ensembles of protein structures and their dynamics using cryo-EM at molecular to near-atomic level. Compared with other methods, cryo-EM covers a larger range of molecular weights and sample conditions. Even the structure of proteins inside the cell can now be analyzed in situ by FIB-milling or cryo-sectioning. Cryo-EM, a just recently matured technique, is a strong contender to contribute novel insights for the study of molecular dynamics of proteins in the future.

Transparency Document

The http://dx.doi.org/10.1016/j.bbagen.2017.07.020 associated with this article can be found in the online version.

Acknowledgements

We acknowledge support from a Grant-in-Aid for Scientific Research on Innovative Areas (JP16H00786 to KM) from MEXT of Japan, and for direct funding by the Japanese government to OIST.

References

[1] M. Adrian, J. Dubochet, J. Lepault, M.W. Adrian, Cryo-electron microscopy of viruses, Nature 308 (1984) 32–36.
[2] J. Dubochet, M. Adrian, J. Chang, J. Homo, J. Lepault, A. McDowall, P. Schultz, Cryo-electron microscopy of vitrified specimens, Q. Rev. Biophys. 21 (1988) 129–228.
[3] R. Henderson, The potential and limitations of neutrons, electrons and X-rays for atomic resolution microscopy of unstained biological molecules, Q. Rev. Biophys. 28 (1995) 171–193.
[4] L.A. Baker, J.L. Rubinstein, Radiation damage in electron cryomicroscopy, Methods Enzymol. 481 (2010) 371–388.
[5] A. Merk, A. Bartesaghi, S. Banerjee, V. Falconieri, P. Rao, M.I. Davis, R. Pragani, M.B. Boxer, L.A. Earl, J.L.S. Milne, S. Subramaniam, Breaking Cryo-EM resolution barriers to facilitate drug discovery, Cell 165 (2016) 1698–1707.
[6] M. Khoshouei, M. Radjainia, W. Baumeister, R. Danev, Cryo-EM structure of haemoglobin at 3.2 A determined with the Volta phase plate, Nat. Commun. 8 (2017) 1–6.
[7] Y. Fujiyoshi, Low dose techniques and cryo-electron microscopy, Methods Mol. Biol. 955 (2013) 103–118.
[8] K. Thurmer, S. Nie, Formation of hexagonal and cubic ice during low-temperature growth, Proc. Natl. Acad. Sci. 110 (2013) 11757–11762.
[9] M. Cyrklaff, W. Kiihlbrandt, High-resolution Electron Microscopy of Biological Specimens in Cubic Ice, Ultramicroscopy 55 (1994) 141–153.
[10] W. Chiu, E. Knapek, T.W. Jeng, I. Dietrich, Electron Radiation Damage of a Thin Protein Crystal at 4 K, Ultramicroscopy 6 (1981) 291–295.
[11] R.M. Glaeser, Retrospective: radiation damage and its associated "information limitations", J. Struct. Biol. 163 (2008) 271–276.
[12] B.E. Bammes, J. Jakana, M.F. Schmid, W. Chiu, Radiation damage effects at four specimen temperatures from 4 to 100 K, J. Struct. Biol. 169 (2010) 331–341.
[13] C.V. Iancu, E.R. Wright, J.B. Heymann, G.J. Jensen, A Comparison of Liquid Nitrogen and Liquid Helium as Cryogens for Electron Cryotomography, J. Struct. Biol. 153 (2006) 231–240.
[14] L.R. Comolli, K.H. Downing, Dose Tolerance at Helium and Nitrogen Temperatures for Whole Cell Electron Tomography, J. Struct. Biol. 152 (2005) 149–156.
[15] A.F. Brilot, J.Z. Chen, A. Cheng, J. Pan, S.C. Harrison, C.S. Potter, B. Carragher, R. Henderson, N. Grigorieff, H. Em, Beam-induced motion of vitrified specimen on holey carbon film, J. Struct. Biol. 177 (2012) 630–637.
[16] X. Li, P. Mooney, S. Zheng, C.R. Booth, M.B. Braunfeld, S. Gubbens, D.A. Agard, Y. Cheng, Electron counting and beam-induced motion correction enable near-atomic-resolution single-particle cryo-EM, Nat. Methods 10 (2013) 584–590.
[17] W. Kühlbrandt, The resolution revolution, Science 343 (2014) 1443–1444.
[18] C. Bernecky, F. Herzog, W. Baumeister, J.M. Plitzko, P. Cramer, Structure of transcribing mammalian RNA polymerase II, Nature 529 (2016) 551–554.
[19] R.A. Grassucci, D.J. Taylor, J. Frank, Preparation of macromolecular complexes for cryo-electron microscopy, Nat. Protoc. (2007) 3239–3246.
[20] D.F. Kelly, D. Dukovski, T. Walz, Strategy for the use of affinity grids to prepare non-his-tagged macromolecular complexes for single-particle electron microscopy, J. Mol. Biol. 400 (2010) 675–681.
[21] W.F. Tivol, A. Briegel, J.G. Jensen, An improved cryogen for plunge freezing, Microsc. Microanal. 14 (2008) 375–379.
[22] T. Jain, P. Sheehan, J. Crum, B. Carragher, C.S. Potter, Spotiton: a prototype for an integrated inkjet dispense and vitrification system for cryo-TEM, J. Struct. Biol. 179 (2012) 68–75.
[23] I. Razinkov, V.P. Dandey, H. Wei, Z. Zhang, D. Melnekoff, W.J. Rice, C. Wigge, C.S. Potter, B. Carragher, A new method for vitrifying samples for cryoEM, J. Struct. Biol. 195 (2016) 190–198.
[24] A. Rohou, N. Grigorieff, CTFFIND4: fast and accurate defocus estimation from electron micrographs, J. Struct. Biol. 192 (2015) 216–221.
[25] K. Zhang, Gctf: real-time CTF determination and correction, J. Struct. Biol. 193 (2016) 1–12.
[26] J.M. Bell, M. Chen, P.R. Baldwin, S.J. Ludtke, High resolution single particle refinement in EMAN2.1, Methods 100 (2016) 25–34.
[27] G. Tang, L. Peng, P.R. Baldwin, D.S. Mann, W. Jiang, I. Rees, S.J. Ludtke, EMAN2: an extensible image processing suite for electron microscopy, J. Struct. Biol. 157 (2007) 38–46.
[28] S.H.W. Scheres, RELION: implementation of a Bayesian approach to cryo-EM structure determination, J. Struct. Biol. 180 (2012) 519–530.
[29] J.M. de la Rosa-Trevin, A. Quintana, L. del Cano, A. Zaldivar, I. Foche, J. Gutierrez, J. Gomez-Blanco, J. Burguet-Castell, J. Cuenca-Alba, V. Abrishami, J. Vargas, J. Oton, G. Sharov, J.L. Vilas, J. Navas, P. Conesa, M. Kazemi, R. Marabini, C.O.S. Sorzano, J.M. Carazo, Scipion: a software framework toward integration, reproducibility and validation in 3D electron microscopy, J. Struct. Biol. 195 (2016) 93–99.
[30] A.M. Roseman, FindEM - a fast, efficient program for automatic selection of particles from electron micrographs, J. Struct. Biol. 145 (2004) 91–99.
[31] J.Z. Chen, N. Grigorieff, SIGNATURE: a single-particle selection system for molecular electron microscopy, J. Struct. Biol. 157 (2007) 168–173.
[32] F.J. Sigworth, A maximum-likelihood approach to single-particle image refinement, J. Struct. Biol. 122 (1998) 328–339.
[33] D. Lyumkis, A.F. Brilot, D.L. Theobald, N. Grigorieff, Likelihood-based classification of cryo-EM images using FREALIGN, J. Struct. Biol. 183 (2013) 377–388.
[34] N. Grigorieff, Frealign: an exploratory tool for single-particle Cryo-EM, Methods Enzymol. 579 (2016) 191–226.
[35] T. Moriya, M. Saur, M. Stabrin, F. Merino, H. Voicu, Z. Huang, P.A. Penczek, S. Raunser, C. Gatsogiannis, High-resolution single particle analysis from electron cryo-microscopy images using SPHIRE, J. Vis. Exp. 123 (2017) e55448.
[36] A. Punjani, J.L. Rubinstein, D.J. Fleet, M.A. Brubaker, cryoSPARC: algorithms for rapid unsupervised cryo-EM structure determination, Nat. Methods 14 (2017) 290–296.
[37] J. Frank, Three-dimensional Electron Microscopy of Macromolecular Assemblies: Visualization of Biological Molecules in their Native State, Oxford Univerity Press, New York, 2006.
[38] R.A. Crowther, D.J. DeRosier, F.R.S. Klug, The reconstruction of a three-dimensional structure from projections and its application to electron microscopy, Proc. R. Soc. Lond. A 317 (1970) 310–340.
[39] G.T. Herman, Image Reconstruction from Projections: The Fundamentals of Computerized Tomography, Academic Press, New York, 1980.
[40] G.A. Frank, A. Bartesaghi, O. Kuybeda, M.J. Borgnia, T.A. White, G. Sapiro, S. Subramaniam, Computational separation of conformational heterogeneity using cryo-electron tomography and 3D sub-volume averaging, J. Struct. Biol. 178 (2012) 165–176.
[41] S. Phan, D. Boassa, P. Nguyen, X. Wan, J. Lanman, A. Lawrence, M.H. Ellisman, 3D reconstruction of biological structures: automated procedures for alignment and reconstruction of multiple tilt series in electron tomography, Adv. Struct. Chem. Imaging 2 (2016) 1–18.
[42] W.J.H. Hagen, W. Wan, J.A.G. Briggs, Implementation of a cryo-electron tomography tilt-scheme optimized for high resolution subtomogram averaging, J. Struct. Biol. 197 (2017) 191–198.
[43] M. Stölken, F. Beck, T. Haller, R. Hegerl, I. Gutsche, J.M. Carazo, W. Baumeister, S.H.W. Scheres, S. Nickell, Maximum likelihood based classification of electron tomographic data, J. Struct. Biol. 173 (2011) 77–85.
[44] D. Kimanius, B.O. Forsberg, S. Scheres, E. Lindahl, Accelerated cryo-EM structure determination with parallelisation using GPUs in RELION-2, elife 5 (2016) e18722.
[45] F.K.M. Schur, M. Obr, W.J.H. Hagen, W. Wan, A.J. Jakobi, J.M. Kirkpatrick, C. Sachse, H. Kräusslich, J.A.G. Briggs, An atomic model of HIV-1 capsid-SP1 reveals structures regulating assembly and maturation, Science 353 (2016) 506–508.
[46] S. Asano, Y. Fukuda, F. Beck, A. Aufderheide, F. Förster, R. Danev, W. Baumeister, W, Proteasomes. A molecular census of 26S proteasomes in intact neurons, Science 347 (2015) 439–442.
[47] R. Henderson, Avoiding the Pitfalls of Single Particle Cryo-electron Microscopy: Einstein from Noise, Proc. Natl. Acad. Sci. 110 (2013) 18037–18041.
[48] A. Briegel, M. Pilhofer, D.N. Mastronarde, G.J. Jensen, The challenge of determining handedness in electron tomography and the use of DNA origami gold nanoparticle helices as molecular standards, J. Struct. Biol. 183 (2013) 95–98.
[49] V. Migunov, H. Ryll, X. Zhuge, M. Simson, L. Strüder, K.J. Batenburg, L. Houben, R.E. Dunin-Borkowski, Rapid low dose electron tomography using a direct electron detection camera, Sci Rep 5 (2015) 14516.
[50] M.J. Berardi, W.M. Shih, S.C. Harrison, J.J. Chou, Mitochondrial uncoupling protein 2 structure determined by NMR molecular fragment searching, Nature 476 (2011) 109–113.
[51] M. Van Heel, M. Schatz, Fourier shell correlation threshold criteria, J. Struct. Biol. 151 (2005) 250–262.
[52] P.B. Rosenthal, R. Henderson, Optimal determination of particle orientation, absolute hand, and contrast loss in single-particle electron cryomicroscopy, J. Mol. Biol. 333 (2003) 721–745.
[53] A. Kucukelbir, F.J. Sigworth, H.D. Tagare, Quantifying the Local Resolution of Cryo-EM Density Maps, Nat. Methods. 11 (2014).
[54] G. Cardone, J.B. Heymann, A.C. Steven, One number does not fit all: mapping local variations in resolution in cryo-EM reconstructions, J. Struct. Biol. 184 (2013) 226–236.
[55] P. Emsley, K. Cowtan, Coot: model-building tools for molecular graphics, Acta Crystallogr. Sect. D: Biol. Crystallogr. 60 (2004) 2126–2132.
[56] T.A. Jones, Interactive electron-density map interpretation: from INTER to O, Acta Crystallogr. Sect. D 60 (2004) 2115–2125.
[57] A. Brown, F. Long, A. Robert, J. Toots, P. Emsley, Research Papers Tools for Macromolecular Model Building and Refinement into Electron Cryo-microscopy Reconstructions Research, Acta Crystallogr. Sect. D Biol. Crystallogr. 71 (2015) 136–153.
[58] N. Echols, N.W. Moriarty, H.E. Klei, P.V. Afonine, G. Bunkóczi, J.J. Headd, A.J. McCoy, R.D. Oeffner, R.J. Read, T.C. Terwilliger, P.D. Adams, Automating crystallographic structure solution and refinement of protein-ligand complexes, Acta Crystallogr. Sect. D: Biol. Crystallogr. 70 (2014) 144–154.
[59] B.J. Bender, A. Cisneros, A.M. Duran, J.A. Finn, D. Fu, A.D. Lokits, B.K. Mueller, A.K. Sangha, M.F. Sauer, A.M. Sevy, G. Sliwoski, J.H. Sheehan, F. DiMaio, J. Meiler, R. Moretti, Protocols for molecular modeling with Rosetta3 and RosettaScripts, Biochemistry 55 (2016) 4748–4763.
[60] B. Webb, A. Sali, Comparative protein structure modeling using MODELLER, Curr. Protoc. Bioinforma 54 (2016) 5.6.1–5.6.32.
[61] Q. Jin, C.O.S. Sorzano, J.M. De La Rosa-Trevín, J.R. Bilbao-Castro, R. Núñez-Ramírez, O. Llorca, F. Tama, S. Jonić, Iterative elastic 3D-to-2D alignment method using normal modes for studying structural dynamics of large macromolecular complexes, Structure 22 (2014) 496–506.
[62] R.S. Ruskin, Z. Yu, N. Grigorieff, Quantitative characterization of electron detectors for transmission electron microscopy, J. Struct. Biol. 184 (2013) 385–393.
[63] G.C. Lander, S.M. Stagg, N.R. Voss, A. Cheng, D. Fellmann, J. Pulokas, C. Yoshioka, C. Irving, A. Mulder, P.W. Lau, D. Lyumkis, C.S. Potter, B. Carragher, Appion: an integrated, database-driven pipeline to facilitate EM image processing, J. Struct. Biol. 166 (2009) 95–102.
[64] N. Biyani, R.D. Righetto, R. McLeod, D. Caujolle-Bert, D. Castano-Diez, K.N. Goldie, H. Stahlberg, Focus: the interface between data collection and data processing in

cryo-EM, J. Struct. Biol. 198 (2017) 124–133.
[65] S.Q. Zheng, E. Palovcak, J. Armache, K.A. Verba, Y. Cheng, D.A. Agard, MotionCor2: anisotropic correction of beam-induced motion for improved cryo-electron microscopy, Nat. Methods 14 (2017) 331–332.
[66] Z. Ripstein, J. Rubinstein, Chapter Five - Processing of cryo-EM movie data, Methods Enzymol. 579 (2016) 103–124.
[67] F. Zernike, How I discovered phase contrast, Science 121 (1955) 345–349.
[68] R. Danev, K. Nagayama, Transmission Electron Microscopy with Zernike Phase Plate, Ultramicroscopy 88 (2001) 243–252.
[69] R. Danev, W. Baumeister, Cryo-EM single particle analysis with the volta phase plate, elife 5 (2016) e13046.
[70] R.M. Glaeser, Invited review article: methods for imaging weak-phase objects in electron microscopy, Rev. Sci. Instrum. 84 (2013) 111101.
[71] R. Danev, D. Tegunov, W. Baumeister, Using the Volta phase plate with defocus for cryo-EM single particle analysis, elife 6 (2017) e23006.
[72] R.F. Egerton, Electron energy-loss spectroscopy in the TEM, Rep. Prog. Phys. 72 (2009) 16502.
[73] Y. Fukuda, U. Laugks, V. Lučić, W. Baumeister, R. Danev, Electron cryotomography of vitrified cells with a Volta phase plate, J. Struct. Biol. 190 (2015) 143–154.
[74] C. Suloway, J. Pulokas, D. Fellmann, A. Cheng, F. Guerra, J. Quispe, S. Stagg, C.S. Potter, B. Carragher, Automated molecular microscopy: the new Leginon system, J. Struct. Biol. 151 (2005) 41–60.
[75] D.N. Mastronarde, Automated electron microscope tomography using robust prediction of specimen movements, J. Struct. Biol. 152 (2005) 36–51.
[76] X. Li, S. Zheng, D.A. Agard, Y. Cheng, Asynchronous data acquisition and on-the-fly analysis of dose fractionated cryoEM images by UCSFImage, J. Struct. Biol. 192 (2015) 174–178.
[77] X. Li, N. Grigorieff, Y. Cheng, GPU-enabled FREALIGN: accelerating single particle 3D reconstruction and refinement in Fourier space on graphics processors, J. Struct. Biol. 172 (2010) 407–412.
[78] S.G. Wolf, L. Houben, M. Elbaum, Cryo-scanning transmission electron tomography of biological cells, Nat. Methods 11 (2014) 423–428.
[79] J. Zhao, S. Benlekbir, J. Rubinstein, Electron cryomicroscopy observation of rotational states in a eukaryotic V-ATPase, Nature 521 (2015) 241–245.
[80] A. Bartesaghi, A. Merk, S. Banerjee, D. Matthies, X. Wu, J.L.S. Milne, S. Subramaniam, 2.2 Å resolution cryo-EM structure of β-galactosidase in complex with a cell-permeant inhibitor, Science 348 (2015) 1147–1151.
[81] J. Frank, A. Ourmazd, Continuous changes in structure mapped by manifold embedding of single-particle data in cryo-EM, Methods 100 (2016) 61–67.
[82] A. Dashti, P. Schwander, R. Langlois, R. Fung, W. Li, A. Hosseinizadeh, H.Y. Liao, J. Pallesen, G. Sharma, V. Stupina, A.E. Simon, J.D. Dinman, J. Frank, A. Ourmazd, Trajectories of the ribosome as a Brownian nanomachine, Proc. Natl. Acad. Sci. 111 (2014) 17492–17497.
[83] A.B. Loveland, G. Demo, N. Grigorieff, A.A. Korostelev, Ensemble cryo-EM elucidates the mechanism of translation fidelity, Nature 546 (2017) 113–117.
[84] Y. Gao, E. Cao, D. Julius, Y. Cheng, TRPV1 structures in nanodiscs reveal mechanisms of ligand and lipid action, Nature 534 (2016) 347–351.
[85] J.A.G. Briggs, Structural biology in situ-the potential of subtomogram averaging, Curr. Opin. Struct. Biol. 23 (2013) 261–267.
[86] V. Lučić, A. Rigort, W. Baumeister, Cryo-electron tomography: the challenge of doing structural biology in situ, J. Cell Biol. 202 (2013) 407–419.
[87] J. Liu, A. Bartesaghi, M.J. Borgnia, G. Sapiro, S. Subramaniam, Molecular architecture of native HIV-1 gp120 trimers, Nature 455 (2008) 109–113.
[88] Y.W. Chang, L.A. Rettberg, A. Treuner-Lange, J. Iwasa, L. Sogaard-Andersen, G.J. Jensen, Architecture of the type IVa pilus machine, Science 351 (2016) aad2001.
[89] A. Briegel, P. Ames, J.C. Gumbart, C.M. Oikonomou, J.S. Parkinson, G.J. Jensen, The mobility of two kinase domains in the *Escherichia coli* chemoreceptor array varies with signalling state, Mol. Microbiol. 89 (2013) 831–841.
[90] C.K. Cassidy, B.A. Himes, F.J. Alvarez, J. Ma, G. Zhao, J.R. Perilla, K. Schulten, P. Zhang, CryoEM and computer simulations reveal a novel kinase conformational switch in bacterial chemotaxis signaling, elife 4 (2015) e08419.
[91] B. Hu, W. Margolin, I.J. Molineux, J. Liu, Structural remodeling of bacteriophage T4 and host membranes during infection initiation, Proc. Natl. Acad. Sci. 112 (2015) E4919–E4928.
[92] X. Liu, Q. Zhang, K. Murata, M.L. Baker, M.B. Sullivan, C. Fu, M.T. Dougherty, M.F. Schmid, M.S. Osburne, S.W. Chisholm, W. Chiu, Structural changes in a marine podovirus associated with release of its genome into *Prochlorococcus*, Nat. Struct. Mol. Biol. 17 (2010) 830–836.
[93] K. Murata, Q. Zhang, J. Gerardo Galaz-Montoya, C. Fu, M.L. Coleman, M.S. Osburne, M.F. Schmid, M.B. Sullivan, S.W. Chisholm, W. Chiu, Visualizing adsorption of Cyanophage P-SSP7 onto marine *Prochlorococcus*, Sci Rep 7 (2017) 44176.
[94] X. Yu, D. Veesler, M.G. Campbell, M.E. Barry, F.J. Asturias, M.A. Barry, V.S. Reddy, Cryo-EM structure of human adenovirus D26 reveals the conservation of structural organization among human adenoviruses, Sci. Adv. 3 (2017) e1602670.
[95] X. Agirrezabala, E. Samatova, M. Klimova, M. Zamora, D. Gil-carton, M.V. Rodnina, M. Valle, Ribosome Rearrangements at the Onset of Translational Bypassing, Sci. Adv. 3 (2017) e1700147.